Simulations reveal slow detachment and fast reattachment of kinesin and dynein in antagonistic pairs

Tzu-Chen Ma, Allison M. Gicking, Qingzhou Feng, and William O. Hancock

Department of Biomedical Engineering, Pennsylvania State University, University Park, PA 16802

Abstract:

Intracellular transport is propelled by kinesin and cytoplasmic dynein motors that carry membrane-bound vesicles and organelles bidirectionally along microtubule tracks. Much is known about these motors at the molecular scale, but many questions remain regarding how kinesin and dynein cooperate and compete during bidirectional cargo transport at the cellular level. The goal of the present study was to use a stochastic stepping model to identify specific motor properties that determine the speed, directionality, and transport dynamics of a cargo carried by one kinesin and one dynein motor. The computational model incorporated load-dependent properties of kinesin-1 and dynein-dynactin-BicD2 (DDB) taken from published optical tweezer experiments. Model performance was evaluated by comparing simulations to recently published experiments of kinesin-DDB pairs connected by complementary oligonucleotide linkers. Using motor parameters from single molecule studies, the simulations recapitulated mean experimental cargo velocities, but displayed considerable directional switching and positional fluctuations not seen in experiments. Instantaneous velocity distributions from kinesin-DDB experiments showed a single peak centered around zero, whereas simulated velocity distributions showed a slow plus-end directional velocity peak and two additional peaks corresponding to fast unloaded kinesin and DDB velocities. We hypothesized that directional switching in the simulations resulted from frequent motor detachment events and non-negligible durations during which only one motor is attached. To investigate this hypothesis, we explored how specific parameters in the model contributed to the overall cargo dynamics and found that making DDB detachment insensitive to load and increasing the kinesin-1 reattachment rate to 50 s^{-1}, together with small adjustments in the kinesin stall force and cargo stiffness brought the simulations into alignment with the experiments. These results provide new insights into motor dynamics during bidirectional transport and put forth hypotheses that can be tested by future experiments.

Statement of significance:

Bidirectional transport of vesicles along microtubules is vital for cellular function, particularly in the highly elongated axons and dendrites of neurons, and transport defects are linked to neurodegenerative diseases. For developing future therapeutic strategies, a better understanding is needed for how motors, cargo adapters, and accessory proteins coordinate their activities to transport cargo to their proper cellular locations. We approached this problem by simulating how antagonistic kinesin and dynein motors compete in pairs. We constrain our simulations by recent experimental results and conclude that the motors spend nearly all their time attached to the microtubule and competing against one another. This behavior is not predicted by existing single-molecule experiments and thus provides new insights into bidirectional transport.

Introduction:

Kinesin and dynein motor proteins carry out anterograde and retrograde transport in cells (1,2) and work together to achieve long-distance bidirectional transport in neurons (3). Coordinated transport is important for neuron growth and function (4-6), and dysfunction can lead to neurodegenerative diseases like ALS and Alzheimer's (5,7,8). However, the mechanisms through which kinesin and dynein cooperate during cargo transport are unclear. Tracking of vesicles and other cargo in cells can reveal the complex dynamics of bidirectional transport (9-13), but this approach does not allow direct observation of the motors involved, and interpretations are complicated by the many regulatory factors that control intracellular transport (6). Single particle tracking and optical tweezer studies have uncovered key details of the mechanisms by which individual motor proteins walk along microtubules (14-16), but apart from a few exceptions, experiments involving antagonistic motor pairs or teams are lacking. Computational simulations provide a valuable tool to bridge the gap between single-motor studies in vitro and cargo transport observations in cells, and these approaches help to uncover aspects of motor function that are difficult to observe through experiments.

A number of stochastic stepping models have been developed to simulate microtubule-based transport by kinesin and dynein motors (17-22). These models are parameterized based on single-particle tracking and optical tweezer experiments, and the simulation results can be used to investigate the influence of specific motor parameters on the resulting bidirectional transport directionality and speed. However, one challenge is that bidirectional cargo trajectories are inherently complex and involve both directional switching and fluctuating velocities, making it difficult to quantitatively compare simulations and experiments. A second challenge is that simulation results are highly dependent on choices of specific parameters that describe motor stepping and motor-microtubule binding/unbinding kinetics, and in many cases these parameters are not tightly constrained by existing experiments.

There have been several experimental developments over the last few years that motivate the next generation of bidirectional stepping models. The first is the appreciation that traditional single-bead optical tweezers create non-negligible vertical forces normal to the microtubule that can accelerate the detachment of kinesin under load (23). This effect was clearly demonstrated by the finding that, compared to the single-bead assay, the kinesin-1 (Kin-1) attachment duration at stall increases substantially in a three-bead assay, where vertical forces are eliminated (24). The second major development is the finding that cytoplasmic dynein activated by cargo adaptors such as BicD2, BicDR1, and Hook3 is highly processive and can generate forces in the range of kinesins (25-32). A third important discovery was that activated

dynein complexes such as dynein-dynactin-BicD2 (DDB) frequently switch between three motility states – processive, paused, and diffusive – when engaged with a microtubule (27,30,33). Computational simulations provide an important tool to unravel how these different factors play into the bidirectional transport achieved by pairs or teams of kinesin and dynein motors.

The goal of present work is to incorporate recent Kin-1 and DDB experimental insights into a stochastic stepping model that recapitulates the bidirectional transport behavior of single kinesin and DDB motor pairs. Parameter sensitivity tests explored the influence of DDB state-switching and load-dependent detachment behavior as well as the impact of load-dependent detachment and reattachment rates on the resulting bidirectional transport dynamics. The simulations were tuned to match recent in vitro experiments that tracked the dynamics of kinesin-DDB (Kin-DDB) pairs connected through complementary DNA hybridization. We found that incorporating detachment and reattachment rates inferred from published work resulted in directional switching and fast plus- and minus-end velocities not observed in the experiments. Instead, experimental data were best recapitulated by a model that incorporated a load insensitive detachment rate for DDB and a fast reattachment rate for Kin-1. Thus, these simulations predict that motors working in antagonistic pairs have different properties than motors in isolation, and these properties enhance competition between kinesin and dynein.

Methods:

Bidirectional transport stochastic stepping algorithm:

Kin-DDB bidirectional transport was simulated using an updated and modified version of a previously published model (20). At each timepoint, any attached motor can step forward by 8 nm, step backward by 8 nm, or detach from the microtubule; any detached motor can reattach to the microtubule. In the DDB switching model, an attached DDB motor can also switch between processive, diffusive, and stuck states. The decision for what event occurs and the time of the transition is decided by time evolution of the system using the Gillespie Stochastic Simulation Algorithm (34), as follows. For an event with a first-order transition rate constant, *k*, the transition times were generated as:

$$t = \frac{1}{k} \ln \frac{1}{R}$$

where R is a uniformly distributed random number in range 0 to 1. In a system with N events the rate of any event occurring equals the sum of the rate constants for all of the possible events, as follows:

$$t = \frac{1}{\sum_{i=1}^{N} k_i} \ln \frac{1}{R}$$

The probability of event *i* occurring is proportional to it rate constant, thus:

$$P_i = \frac{k_i}{\sum_{i=1}^{N} k_i}$$

At each time-point, a random number is used to determine the time to the next transition, and then a second random number is chosen to determine which transition will occur.

Kinesin-1 simulation parameters

Force is defined as positive in the plus-end direction and negative in the minus-end direction; thus, for Kin-1 negative forces are hindering and positive forces are assisting loads. Based on the Kin-DDB bidirectional transport model, the load, *F*, applied on each motor was defined by the distance between cargo and motor multiplied by stiffness of the motor.

$$F = \kappa_{stiff} * \Delta x$$

Here, κ_{stiff} is the stiffness of the motor and Δx is the distance between cargo and the head domain of the motor. In our previous model, we used $\kappa_{stiff}^{kin} = 0.3$ pN/nm and $\kappa_{stiff}^{DDB} = 0.065$ pN/nm (20). For testing the stiffness in the present work, we simplified the model by incorporating an identical stiffness $\kappa_{stiff} = 0.1068$ pN/nm for each motor, which makes the cargo located at a midpoint between two motors' position, in the basic model, based on published work (35-37). The calculation is as follows,

$$\kappa_{stiff} = 2 * (\kappa_{stiff}^{kin} * \kappa_{stiff}^{DDB})/(\kappa_{stiff}^{kin} + \kappa_{stiff}^{DDB})$$

The Kin-1 stepping model followed load-dependent velocity from Andreasson et al. (38,39), in which, kinesin velocity remains constant under assisting load and keeps decreasing to zero until under stall force under hindering load, and there is a constant backstepping rate, k_{back} of 3 s^{-1}. The forward stepping rate under hindering load was simplified to a linear function, as follows:

$$k_{forward}(F) = k_{forward}^{0} = \frac{V^0}{8} + k_{back}, F > 0$$

$$k_{forward}(F) = (k_{back} - k_{forward}^{0}) * \left(\frac{F}{F_{stall}}\right) + k_{forward}^{0}, F \leq 0$$

Here, $k_{forward}$ is the forward stepping rate, $k_{forward}^{0}$ is the unloaded forward stepping rate, V^0 is the unloaded velocity, and F_{stall} is the stall force.

Motor detachment under load used the Bell's model (40):

$$k_{detach}(F) = k_{detach}^{0} * e^{\frac{F}{F_{detach}}}$$

Based on Andreasson et al. (39), the unloaded detachment rate, k_{detach}^{0} and detachment force parameter F_{detach} are 1.11 s^{-1} and 6.83 pN under hindering loads, and 7.4 s^{-1} and 12.8 pN under assisting loads, respectively.

DDB simulation parameters:

Because DDB steps toward the minus-end, positive forces denote hindering loads and negative forces denote assisting loads. The DDB kinetic model is based on load dependent velocity from Elshenawy et al. (26), with a constant step-size of 8 nm, and a backstepping rate of 15 s^{-1}. The load dependent velocity was modeled as an exponential function, as follows:

138 $$v(F) = v_{min} * [1 - e^{(F_{stall}-F)*\frac{d}{k_B T}}]$$

139 Here v_{min} is the velocity under super stall force, equal to -201 nm/s, d is characteristic distance of 1.5 nm,
140 and F_{stall} is the stall force of 3.6 pN. The forward stepping rate is calculated by:

141 $$k_{forward}(F) = \frac{v(F)}{8} + k_{back}$$

142 For tuning unloaded DDB velocity but maintaining the published stall force, we used the same forward
143 stepping model in kinesin for DDB stepping rate under hindering load, as follows,

144 $$k_{forward}(F) = (k_{back} - k^0_{forward}) * \left(\frac{F}{F_{stall}}\right) + k^0_{forward}, F \geq 0$$

145 The DDB detachment rate, k_{detach}, was modeled with an exponential load dependence (41):

146 $$k_{detach}(F) = k^0_{detach} * e^{\frac{F}{F_{detach}}}$$

147 Here, k^0_{detach} is 0.1 s^{-1} and F_{detach} is 3 pN, based on experimental work from Belyy et al. (25).

148

149 ***DDB state-switching model***

150 Feng et al. showed that DDB switches between processive, diffusive and stuck states during movement
151 (27). To simulate this behavior, three motility states for DDB were integrated into the model, as follows.
152 In the processive state, DDB can move forward, backward, or detach; in the stuck state, DDB cannot move
153 or detach from microtubule; and in the diffusive state, DDB offers no resistance to kinesin movement and
154 can also detach from the microtubule. Transition rates between states were taken from Feng et al., as
155 follows: the processive-to-stuck switching rate was 1.0 s^{-1} with reverse rate of 1.8 s^{-1}; the stuck-to-
156 diffusive switching rate was 0.07 s^{-1} with a reverse rate of 0.33 s^{-1}; and the diffusive-to-processive
157 switching rate was 3.9 s^{-1} with a reverse rate of 0.23 s^{-1} (27).

158

159 ***Data processing***

160 After running the simulations, the raw data were processed to match the experimental conditions (27),
161 as follows. To match the 20 fps frame rate (27), cargo position was averaged over 50 ms windows. To
162 account for uncertainties in fitting the experimental point spread function, a normally distributed error

with an 8 nm standard deviation was added to cargo position at each time point. The instantaneous velocity at each timepoint was calculated by taking three-point slope of positions 50 ms before and after each point.

166 **Results:**

167 ***Formulation of bidirectional stepping model.***

168 In recently published experiments, bidirectional cargo transport was reconstituted in vitro by connecting
169 a truncated kinesin motor and an activated dynein-dynactin-BicD2 (DDB) complex via complementary
170 single stranded DNA oligonucleotides (27). A quantum dot was then linked to a biotin on one end of the
171 DNA (Fig. 1A), and the position of the fluorescent cargo was tracked via total internal reflection
172 fluorescence (TIRF) microscopy at 20 frames per second. Consistent with previous work (26), the resulting
173 traces were found to have longer binding durations to the microtubule and slower velocities than the
174 unloaded motors alone (Fig. 1C & S2B) (27). To simulate this Kin-DDB transport, we used the Gillespie
175 Stochastic Algorithm (34), where at every time point, each motor can step forward, step backward, detach
176 from or reattach to the microtubule, with the probability of each transition being proportional to its first-
177 order rate constant (Fig. 1B).

178 Previous simulations that investigated the tug-of-war between kinesin-1 and kinesin-2 motors and a single
179 dynein motor or DDB complex found that motor stall force is a much weaker determinant of which motor
180 wins the tug-of-war than the kinetics of the load-dependent detachment of the motors (20). Since
181 publication of those simulations, new experimental data have been published that quantify the load-
182 dependent detachment kinetics of Kin-1 and load-dependent velocity kinetics of DDB complexes (26,39).
183 Motivated by these new data, we reformulated our stochastic model for kinesin-dynein tug-of-war and
184 applied it to the new experimental results. In our updated model, the load-dependent detachment rate
185 for both Kin-1 and DDB matches Bell's model (41,42) with parameters based on Andreasson et al. (33,39).
186 The motor detachment rate under load, $k_{detach}(F)$ is:

187 $$k_{detach}(F) = k^0_{detach} * e^{\frac{F}{F_{detach}}}$$

188 Here, F is the load applied to the motor, k^0_{detach} is the unloaded detachment rate, and F_{detach} is the
189 detachment force parameter. The detachment force is $F_{detach} = \frac{k_B T}{\delta}$, where k_B is Boltzmann constant, T
190 is absolute temperature, and δ is a parameter for distance. The parameters differ in the hindering and
191 assisting load directions (38,39).

192 We modeled the stepping and detachment properties of the activated DDB complex based on optical
193 tweezer data from Elshenawy et al. (26). The DDB step size was set to a uniform 8 nm for simplicity, and
194 the load-dependent velocity was defined by a single exponential function that incorporates both load

195 dependent forward stepping and a constant backward stepping rate. The load-dependent forward
196 stepping model for DDB was:

197 $$k_{forward}(F) = k_{forward}^{min} * (1 - e^{\left(\frac{(F_{stall}+F)d}{k_B T}\right)})$$

198 Here, $k_{forward}^{0}$ is the unloaded stepping rate, and F_{stall} is the stall force which causes the motor to have
199 the same probability of stepping forward and backward. The unloaded velocity of DDB was set to 328
200 nm/s based on published work (27). The unloaded velocity of Kin-1 was set to 515 nm/s based on control
201 experiments we conducted for Kin-1 in dynein buffer (Fig. S1B). We used a load-independent backstepping
202 rate of 3 s^{-1} based on previous optical tweezer experiments (38,43). The Kin-1 forward stepping rate varied
203 linearly with hindering loads and was constant under assisting loads.

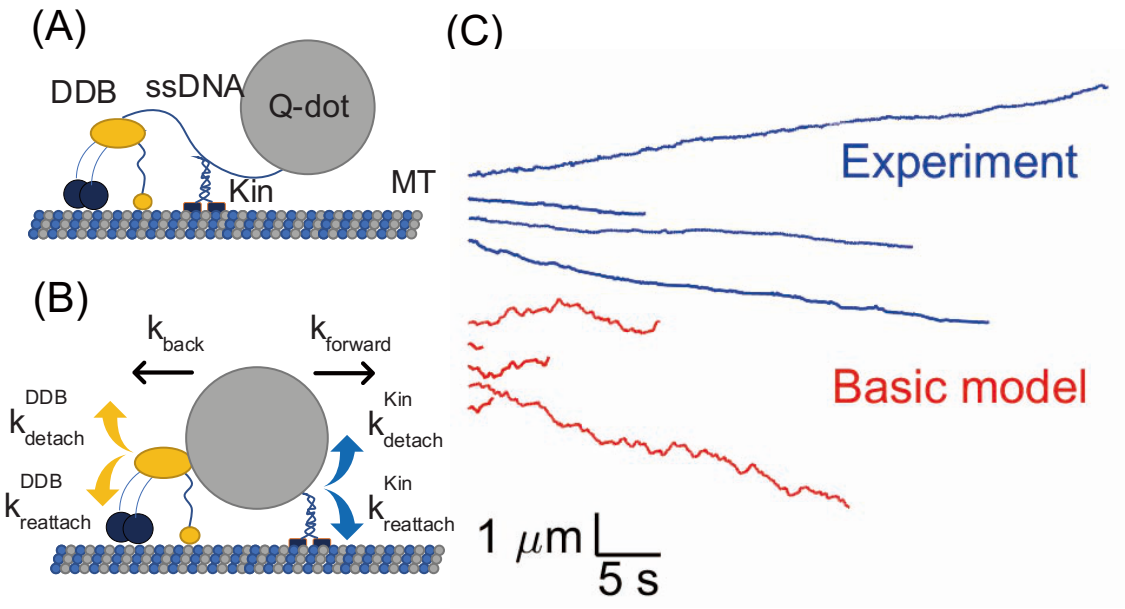

Figure 1. (A) Schematic of kin-DDB bidirectional transport tracking experiment in which motors were connected by a single stranded DNA (ssDNA) and attached to a quantum dot for visualization by fluorescence microscopy (27). (B) Stochastic model of kin-DDB bidirectional transport showing the different rate constants incorporated into the simulations. (C) Example traces of experimental data (blue) from published work (27) and simulation results from the basic model (red).

211 **Comparing bidirectional stepping model simulations to experimental data.**

212 We next simulated bidirectional stepping of a simulated cargo containing one Kin-1 and one DDB motor
213 to determine the degree to which the simulations can recapitulate the experimental results. As shown in
214 Fig. 1C, the mean velocities of the simulations roughly matched the experimental velocities, but the
215 simulated traces contain more long-term minus-end-directed segments and have shorter overall
216 durations than seen in the experiments. Furthermore, the simulated trajectories contain fluctuations and
217 directional switching not seen in the experiments. One explanation for the larger fluctuations in the
218 simulated traces is that experimental temporal and spatial resolution limits are obscuring fluctuations in
219 the experimental data. Therefore, to enable more accurate comparison between experiments and
220 simulations, we added simulated experimental noise and we reduced the temporal resolution to the
221 simulations, as follows. From the quantum dot tracking experiments, we determined the experimental
222 error in the Gaussian fits to the point-spread function to be 8 nm (27), and so we added a normally
223 distributed noise term with a standard deviation of 8-nm to each point in the simulation. Second, we
224 binned the simulated data to 50 ms to match the experimental 20 FPS frame rate of the camera.

225 To better compare the fluctuations in the traces resulting from motor stepping dynamics, we examined
226 5-second segments of experimental and simulated traces. As shown in Fig. 2A, even with the
227 measurement error and time averaging incorporated into the simulations, the simulation traces showed
228 more frequent and larger fluctuations than the experimental traces. These fluctuations were quantified
229 by a Mean Square Displacement (MSD) analysis, which found an apparent diffusion coefficient in
230 experiments of 996 nm^2/s and an apparent diffusion coefficient in simulations of 11,800 nm^2/s (Fig.
231 S1B). To better compare the experimental and simulated velocities, we calculated the instantaneous
232 velocities over 100-ms time windows for both the experimental and simulation results and plotted the
233 instantaneous velocity distributions (Fig. 2B). The experimental instantaneous velocities had a prominent
234 single peak centered at -12 nm/s, and 95% of instantaneous velocities distributed in range between -394
235 to 371 nm/s. In contrast, the simulations had a distinct peak centered around a slow plus-end velocity,
236 and distinct side peaks corresponding to the unloaded velocities of DDB and Kin-1. Using a Gaussian
237 mixture model, the velocity distribution was fit well by three normal distributions: a peak centered at 118
238 nm/s that accounted for 43% of the population, a minor peak at -326 nm/s that accounted for 30% of the
239 population, and another minor peak centered at 178 nm/s that accounted for 27% of the population. The
240 motor reattachment rate in our simulations was 5 s^{-1} based on published experimental data for Kin-1 (44-
241 46), and because equivalent experimental data are not available for dynein, we chose the same value for

242 the DDB complex. This reattachment rate means that when either motor detaches from the microtubule,
243 it will take on average 200 ms to reattach, giving the other motor time to move at its unloaded velocity.
244 Thus, these lateral peaks in the simulated velocity distribution can be explained by the simulations having
245 more periods when only one motor is attached than the experiments.

246 To better understand the underlying motor dynamics that lead to the experimental Kin-DDB traces being
247 relatively smooth and the velocity distribution having a single peak centered around zero, we investigated
248 how the modeled properties of Kin-1 and DDB contribute to the distinctive instantaneous velocity
249 distribution of our 'basic' model described above. We hypothesize that there are properties of Kin-1
250 and/or DDB motors that are different in a two-motor complex than in the single-molecule fluorescence
251 and optical trapping experiments used to develop the basic model. To test this overarching hypothesis,
252 we varied motor parameters and quantified the change in performance, with the goal of reducing the
253 magnitude of the fast plus- and minus-end velocity peaks in the instantaneous velocity histogram (Fig. 2B)
254 to better match the experimental results.

255

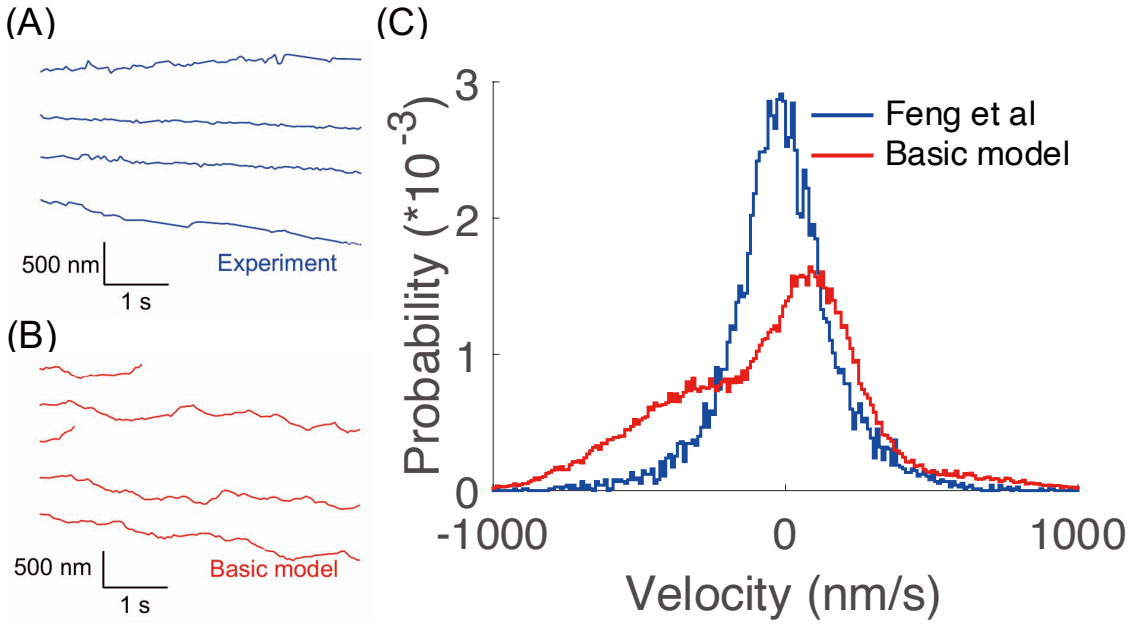

Figure 2. Comparison between simulation results and experimental data from Feng et al. (27). (A and B) Example traces over a 5-second window, showing that simulation traces contain more fluctuations than the experimental traces. (C) Instantaneous velocity distribution (averaged over 100 ms windows), showing three peaks in the simulation results (red), but only a single central peak in the experimental distribution (blue).

263 ***Testing the influence of dynein motor properties on bidirectional transport***

264 The first hypothesis that we tested was that the simulations differ from the experiments because the
265 motile properties of DDB in a bidirectionally moving Kin-DDB complex differ from the properties measured
266 in single-motor DDB optical tweezer experiments. To test this possibility, we investigated whether either
267 altering the load-dependent detachment kinetics of DDB or including experimentally observed pausing
268 and diffusive states of the DDB complex could better align the simulations with the experiments. There is
269 abundant evidence in the literature that dynein alone has catch-bond behavior, meaning that the
270 detachment rate slows down with increasing load (19,22,47-50). To our knowledge, there is no
271 experimental evidence that activated dynein in a DDB complex shows catch bond behavior, but there is
272 only one published study directly addressing this question (26). Thus, we investigated whether the
273 simulated bidirectional behavior is shaped by the load-dependent detachment kinetics of DDB. Because
274 there are many mathematical representations of a catch-bond and there is no agreement in the form for
275 dynein, we settled on an ideal bond, meaning that load has no effect on the DDB detachment rate
276 ($k_{detach}(F) = k^0_{detach}$). When an ideal-bond for DDB was incorporated, the resulting displacement traces
277 model showed no significant improvement in smoothness (Fig. 3A). However, in the instantaneous
278 velocity distribution, removing the load-dependence of DDB detachment shifted the distribution from a
279 three Gaussian mixture to a two Gaussian mixture (Fig. 3C). This change results from the velocity peak
280 associated with unloaded Kin-1 disappearing due to DDB becoming much more difficult to detach from
281 the microtubule. However, the ideal-bond model alone does not resolve the discrepancy with the
282 experimental data because the peak corresponding to unloaded DDB velocity remains.

283 Another property of DDB seen in virtually all published unloaded single-molecule studies is that the DDB
284 complex exhibits long processive runs, but also undergoes episodes of 1D diffusion along the microtubule
285 and spends a significant fraction of the time stuck to the microtubule in an immobilized state (25,27,30,31).
286 Feng et al found that DDB spent 65% of the time in a processive state, 31% of the time in a stuck state,
287 and 4% of the time in a diffusive state, and also quantified the switching rate between states (27). We
288 incorporated this DDB switching behavior into our model and assumed that the diffusive state of DDB
289 offered no resistance to kinesin stepping, and that in the stuck state, DDB neither moved nor detached
290 from microtubule. Like the traces in the ideal-bond model, including state-switching had a minimal effect
291 on the smoothness of the simulated traces (Fig. 3B). In the instantaneous velocity distribution, there was
292 a decrease in the magnitude of the unloaded DDB velocity peak, but almost no effect on the unloaded
293 kinesin velocity peak (Fig 3c). The fall in the unloaded DDB peak can be explained by DDB spending time

294 in the stuck state instead of processive walking. The lack of change in the unloaded kinesin peak is likely
295 due to the fact that DDB is in the diffusive state only a small fraction of the time. It also means that the
296 decrease in the DDB detachment rate resulting from DDB spending time in a stuck state has a weaker
297 effect than incorporating an ideal bond (Fig. 3C). Thus, removing the load-dependence of DDB detachment
298 was able to nearly eliminate the kinesin velocity peak, whereas incorporating a switching model for DDB
299 diminished the unloaded DDB velocity peak. However, neither modification alone could fully reconcile the
300 simulations with the experiments. Thus, to explore other modifications of the model that could diminish
301 the DDB velocity peak, we examined the sensitivity of the model simulations to changes in the kinesin
302 detachment and reattachment rates.

303

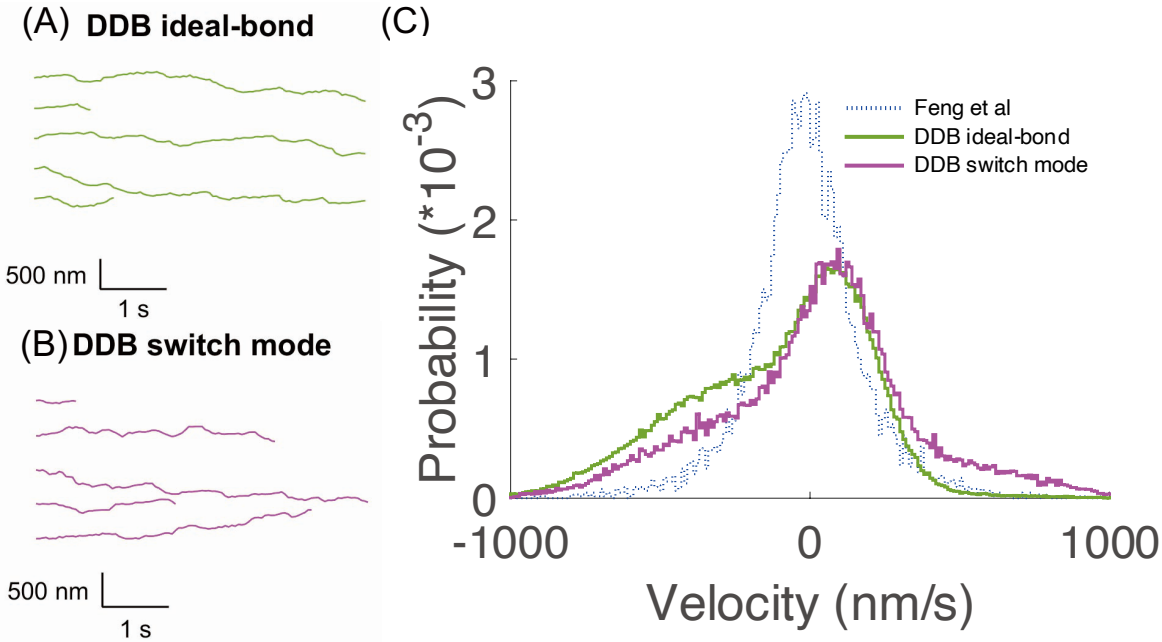

Figure 3. (A and B) Example traces of DDB ideal-bond and DDB switch mode models. (C) Instantaneous velocity distribution from simulations incorporating an ideal bond for DDB (green) and state-switching behavior for DDB (purple). Experimental data from Feng et al. (27) are shown as blue-dotted line.

309 ***Testing the influence of motor attachment and detachment kinetics on bidirectional transport***

310 The second hypothesis we tested was that the discrepancy between simulations and experiments is due
311 to differences in the motor properties of kinesin in an antagonistic motor pair compared to single-bead
312 optical tweezer experiments with isolated kinesin motors. These differences could be due to, for instance,
313 the geometry of a motor attached to trapped bead versus a tight connection to dynein (24), or due to how
314 a detached kinesin remains close to the microtubule due to tethering by dynein. The first approach was
315 to determine whether decreasing the detachment rate of kinesin reduced the magnitude of the DDB
316 velocity peak in the instantaneous velocity distribution. In the load-dependent detachment model,
317 decreasing the detachment rate can be accomplished by either decreasing the unloaded detachment rate,
318 k^0_{detach}, or by decreasing the sensitivity of detachment to load, which is achieved by increasing the
319 detachment force, F_{detach}. We altered these two parameters individually in the simulation and compared
320 results to the experimental data. Decreasing k^0_{detach} substantially decreased the magnitude of the
321 unloaded DDB velocity peak and increased the peak around zero velocity, although it also increased the
322 unloaded kinesin velocity peak (Fig. 4A). Increasing F_{detach} had a similar effect but to a lesser degree (Fig.
323 4B), and the effect plateaued around an F_{detach} value of 35 pN. Thus, decreasing the kinesin detachment
324 rate diminished the minus-end velocity peak, bringing the simulations closer to the experimental results,
325 but neither of these changes had a significant effect on the unloaded kinesin peak.

326 The other way to decrease the fraction of the time Kin-DDB complexes are moving by the action of only
327 one of the two motors is to tune the reattachment rate of each motor. In the basic model, we set a
328 constant reattachment rate, $k_{reattach}$, of 5 s^{-1} for all motors, based on the literature (21,46). To determine
329 whether the kinesin and DDB reattachment rates were contributing to the simulation-experiment
330 mismatch, we tested several larger values of $k_{reattach}$ for each motor. Increasing $k_{reattach}$ for Kin-1
331 strongly diminished the fraction of time the complex moves at the unloaded DDB speed (Fig. 4C), and
332 increased the fraction of time that both motors were engaged, resulting in an enhanced cargo velocity
333 peak near zero. Interestingly, the effect of increasing the Kin-1 $k_{reattach}$ plateaued at a value of 50 s^{-1}. In
334 contrast to Kin-1, increasing $k_{reattach}$ for DDB had only a moderate effect on the fraction of time spent
335 moving at unloaded Kin-1 velocity, likely due to the small size of this plus-end velocity peak, and there
336 was no substantial increase in the velocity peak centered around zero. In summary, changing the Kin-1
337 unloaded detachment rate or reattachment rate had the strongest effect on diminishing the fraction of
338 time the cargo moved near the DDB unloaded velocity, and changing the DDB reattachment rate had little
339 effect.

340

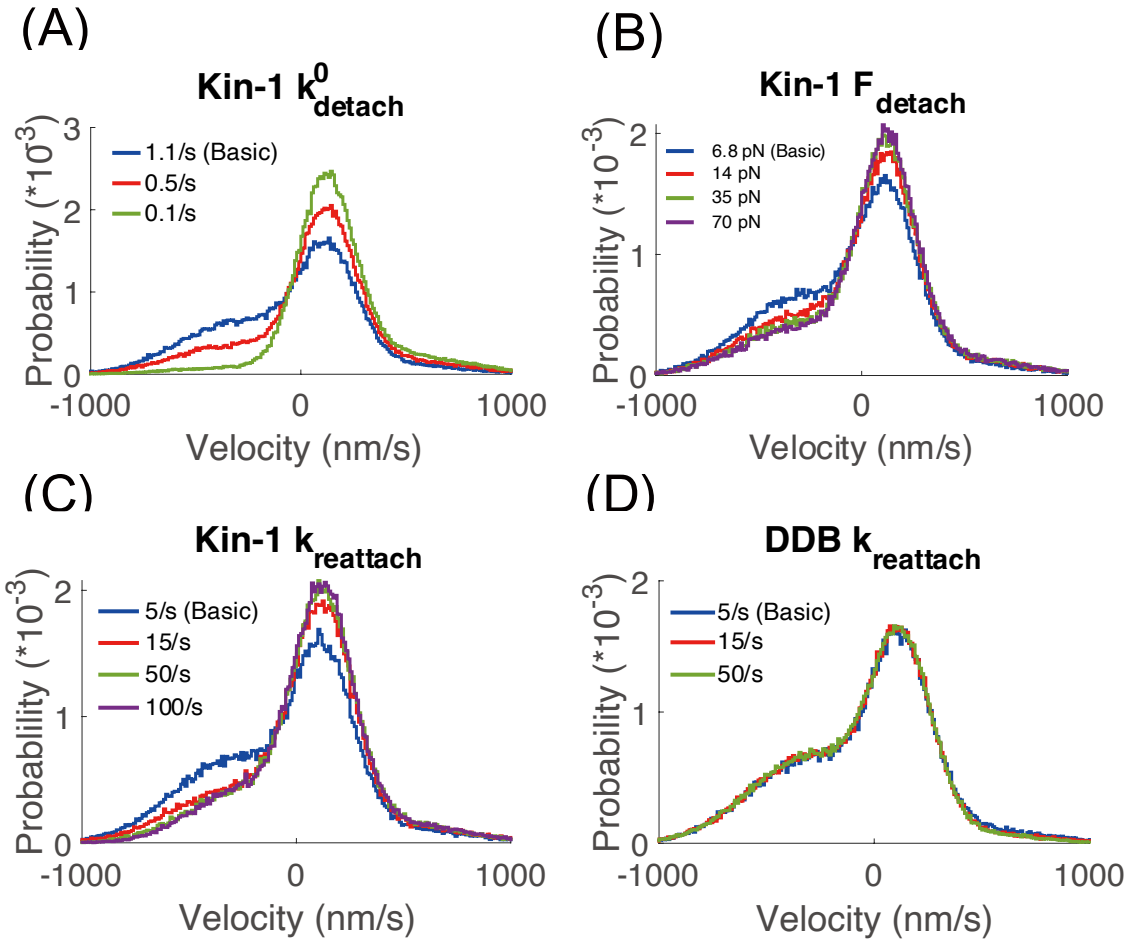

Figure 4. Effect of changing motor attachment and detachment parameters on the instantaneous velocity distribution. (A) Effect of decreasing the unloaded kinesin-1 detachment rate was to diminish the minus-end velocity peak. (B) Effect of increasing the kinesin-1 detachment force parameter was to moderately diminish the minus-end velocity peak. (C) Effect of increasing the kinesin-1 reattachment rate was to diminish the minus-end velocity peak. (D) Changing the DDB reattachment rate had a negligible effect.

348 **Testing influence of motor mechanochemical properties on bidirectional transport**

349 The simulation results to this point showed that altering motor attachment and detachment kinetics can
350 decrease the weight of the distribution corresponding to the two unloaded motor velocities. However,
351 the experimental and model velocity distributions also differed in the location of the central peak, which
352 is centered around zero for the experiments but shifted to a slow plus-end velocity in the basic model (Fig.
353 2C). In contrast to the smaller peaks in the velocity distribution that correspond to kinesin or DDB moving
354 at their unloaded velocity, we hypothesized that the location of this central peak is determined by the
355 chemomechanical properties of the motors when both motors are bound to the microtubule. To test this,
356 we investigated other properties that may have effect on bidirectional transport when both motors bound.

357 We first tested the influence of changing the Kin-1 stall force. In our basic model, the Kin-1 stall force was
358 set to 8 pN and the DDB stall force was set to 3.8 pN based on published optical tweezer experiments
359 (26,38,39). Because of this discrepancy, it not surprising that when both motors are engaged, the kinesin
360 directionality dominates. We tested kinesin stall forces between 4 to 8 pN, which are in the range of
361 different published studies (22,38,51-55), and found that weaker stall forces causes the central velocity
362 peak to shift closer to zero, better matching the experiments (Fig. 5A). The model best matched the
363 experimental data when the stall force was set to 4 pN, but we note that this value is below the majority
364 of published experimental studies.

365 The second property we tested was the DDB backward stepping rate. The backstepping rate of DDB in
366 basic model was 15 s^{-1}, based on optical tweezer experiments of Elshenawy et al. (26). Due to the larger
367 stall force of Kin-1, the DDB backstepping rate is expected to influence the cargo velocity when both
368 motors are engaged and pulling against one another. Interestingly, decreasing the backstepping rate in
369 the simulations had only a small effect on the location of the central velocity peak (Fig. 5B). Furthermore,
370 changing either the stall force of kinesin or the backward stepping rate of DDB had a minimal effect on
371 the weight of side peaks corresponding to kinesin-only and DDB-only velocities.

372 The final property we tested in the simulations was the motor stiffness. We hypothesize that the stiffness
373 may be important because it determines the timecourse of force generation as the motors step in
374 opposite directions; these force generation kinetics then play into the load-sensitive detachment kinetics.
375 Furthermore, when one motor detaches, the spring connecting them will recoil, shifting the cargo back
376 toward the remaining engaged motor. It is difficult to intuit how these effects may shift the velocity
377 distribution, highlighting how the model can build intuition. We found that stiffening both motors had

378 two effects (Fig. 5C): the central velocity peak shifted toward zero and the fastest minus-end velocities
379 were eliminated in the distribution. We attribute this latter change to smaller stiffnesses leading to a
380 'recoil effect' when the kinesin detaches and the cargo rapidly moves toward the minus-end to become
381 centered on the engaged DDB motor.

382

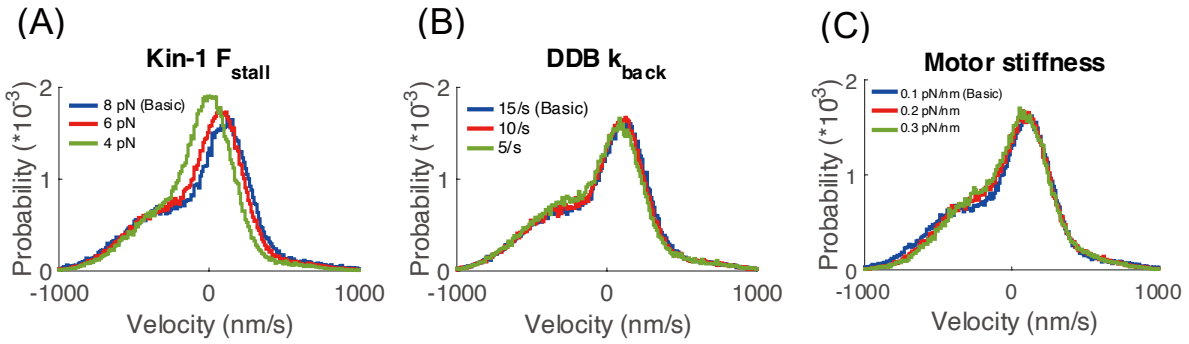

Figure 5. Effect of changing motor mechanochemical properties on the instantaneous velocity distribution. (A) Effect of decreasing the kinesin-1 stall force was to shift the central velocity peak toward zero. (B) Effect of decreasing the DDB backstepping rate was to slightly shift the central peak toward zero. (C) Effect of increasing the motor stiffness was a small shift of the central velocity peak toward zero and a reduction in the fastest minus-end velocities.

389 **Experimental results are best recapitulated by a model with faster kinesin reattachment kinetics and**
390 **load-independent DDB detachment kinetics**

391 From our simulations up to this point, we concluded that identifying an optimal model that better matches
392 the experimental results requires changing more than one parameter. However, a balance must be struck
393 between firmly grounding the model in published experimental single-molecule data and optimizing the
394 agreement between simulations and experimental Kin-DDB results. To navigate this balance, we focused
395 our search on identifying minimal sets of motor parameter modifications that lead to the greatest
396 improvement in the model fits to the experimental data. The parameter adjustments that best minimized
397 the unloaded velocity peaks in the simulations were increasing the reattachment rate of Kin-1 (Fig. 4C)
398 and decreasing the detachment kinetics of both Kin-1 and DDB (Fig. 3A, 4A, and 4B). We chose not to
399 modify the unloaded detachment rate of Kin-1 (Fig. 4A) because single-molecule TIRF measurements from
400 many labs converge on an unloaded Kin-1 detachment rate (equal to velocity divided by run length) in the
401 range of 1 s^{-1} (22,38,39). On the other hand, we felt justified eliminating the load-sensitivity of DDB
402 detachment, given that in optical tweezer experiments, forces up to 6 pN have only a minimal effect on
403 the detachment rate (26), and the detachment rates in those single-bead experiments could be
404 accelerated by vertical forces that are not present in the geometry of our experiments and simulations.
405 Similarly, we felt justified in increasing the reattachment rate of Kin-1 to 50 s^{-1} based on results showing
406 that under load Kin-1 can slip backward and rapidly reengage with the microtubule, indicative of a fast
407 rebinding rate under load (43,56,57).

408 The remaining discrepancy of our 'basic' model with the experimental results was that the central velocity
409 peak was shifted toward the plus-end rather than centered around zero (Fig. 2C). The first modification
410 was to reduce the Kin-1 stall force to 6 pN (Fig. 5A), which is well within the range of experimental values
411 (16,38,51,52). Secondly, we increased the motor stiffness to 0.2 pN/nm (Fig. 5C). This value is reasonable,
412 given that a 6 pN force will stretch this spring 30 nm, which is in the range of the contour lengths of our
413 Kin-1 and DDB constructs. With this 'best-fit' model, we found that the displacement versus time traces
414 were somewhat smoother than the 'basic' model (Fig. 6A), although the fluctuations were still larger than
415 the experimental data (Fig.2A). To quantify this, we carried out MSD analysis. The apparent diffusion
416 coefficient dropped from 11,800 nm^2s^{-1} in the basic model to 1812 nm^2s^{-1} in 'best-fit' model, which was
417 much closer to the 996 nm^2s^{-1} for the experimental data (Fig. S1B). More importantly, in the
418 instantaneous velocity distribution (Fig. 6B), the unloaded velocity peaks, which were a significant
419 discrepancy in the basic model, were nearly eliminated, thus matching the experimental data. The

420 principal mode of the instantaneous velocity distribution in 'best-fit' model was located at 69 nm/s, with
421 95% of instantaneous velocities in the range between -396 to 376 nm/s. Although the central velocity
422 peak was shifted toward zero, the model still did not align fully with the experimental data centered at
423 zero (Fig. 6B). Other features were also improved; for instance, the simulated traces for the 'best fit' model
424 also had longer durations, more closely matching experiments (Fig. S4B). The average velocities computed
425 over each trace were similar on average to both the experimental and the basic model (Fig. 6C), but the
426 distribution of trace velocities was tighter due to the longer run durations (Fig. 6C & S4B). In summary,
427 the experimental Kin-DDB results are best explained by a model in which the DDB detachment rate is
428 independent of load up to the ~6 pN stall forces that kinesin generates, the reattachment rate of kinesin
429 is ten-fold faster or more and motors are stiffer in Kin-DDB complex during transport (Fig. 6D).

430

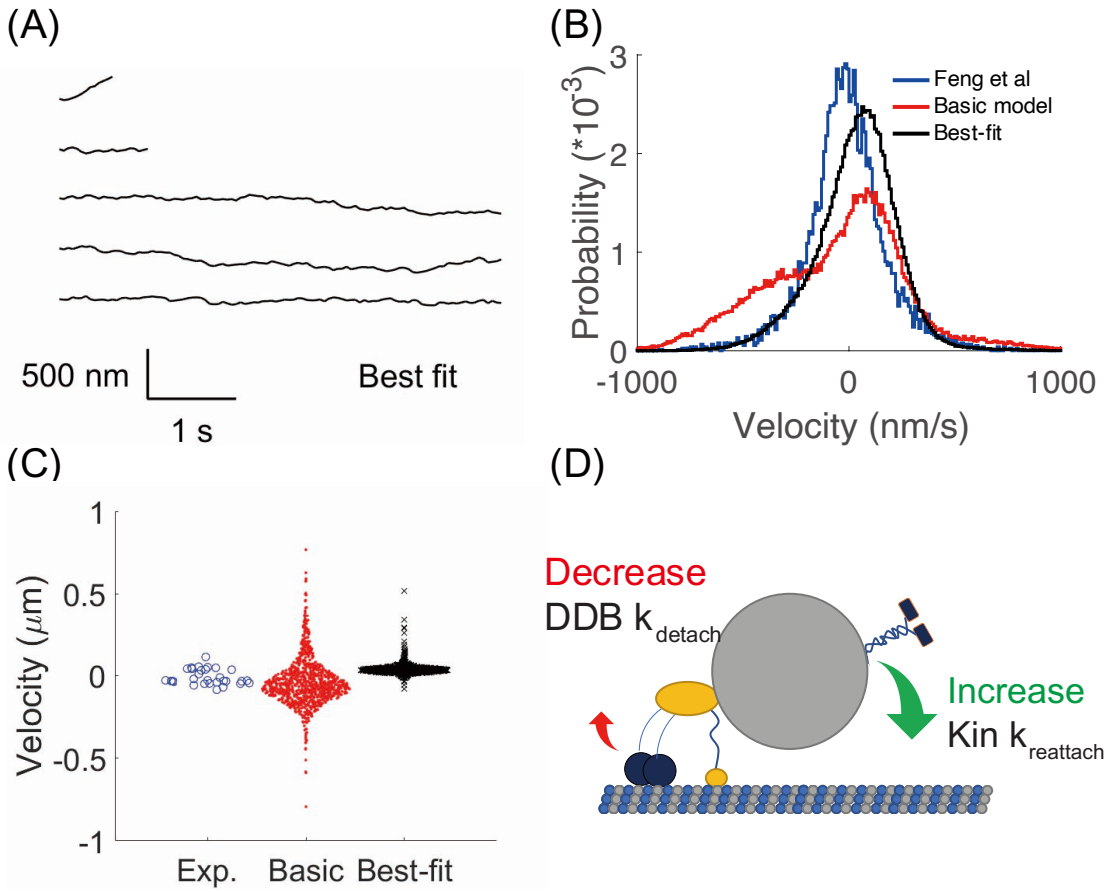

Figure 6. (A) Example traces from best-fit model. (B) Comparison of instantaneous velocity distributions between experimental data (blue), basic model (red) and best-fit model (black). The best-fit model reproduced a single velocity peak similar to experimental data, but the peak was shifted slightly toward the plus-end relative to the experimental data. (C) Comparison of trace velocity distributions for experimental data (blue), basic model (red), and best-fit model (black). (D) Diagram of the best-fit model for kin-DDB bidirectional transport. The detachment rate of DDB is independent of load (ideal-bond) and kinesin-1 reattaches to microtubule with a fast rate ($\geq 50\ s^{-1}$) following detachment. Both of these features maximize the fraction of time both motors are engaged and pulling against one another and minimize durations when only one motor is engaged and moving at its unloaded velocity.

442 **Discussion:**

443 Transport of vesicles in axons and dendrites involves varying numbers and types of motors, as well as
444 regulation at multiple levels. Hence, to understand how kinesin and dynein motors attached to the same
445 cargo compete and coordinate during transport, the field has turned to reconstituting the in vitro motility
446 of pairs of kinesin and activated dynein (1,4,31,46,58). This approach allows an examination of how
447 differing mechanochemical properties of specific motor isotypes translate into effective movement
448 against an antagonistic partner. Consistent behavior of kinesin-dynein pairs that are observed across
449 different labs (25-27,59) include the following: 1) kin-DDB complexes remain bound to microtubules for
450 ~tens of seconds (26,27), considerably longer than Kin-1 or DDB alone; 2) trajectories include episodes,
451 lasting from seconds to tens of seconds, where the velocity of the complex is ~10-fold slower than the
452 unloaded velocities of the respective motors; and 3) cargo trajectories are quite smooth and show few if
453 any directional switches. In principle, it should be possible to recapitulate these motility behaviors using
454 Kin-DDB simulations that incorporate established parameters for kinesin and dynein behavior in isolation.
455 However, we find this not to be the case. Instead, simulations of Kin-DDB transport in our 'basic' model
456 show frequent directional switches and signification proportions of time when the complex moves at the
457 unloaded velocity of the motors (Fig. 2B). The discrepancies between the simulations and experiments
458 were clearly seen by comparing the instantaneous velocity distributions. The experimental data was
459 centered in a wide peak around zero velocity, whereas the simulated data had additional peaks
460 corresponding to the unloaded Kin-1 and DDB velocities, along with a central peak centered around a slow
461 plus-end speed. Thus, we focused our in silico 'experiments' on identifying parameter adjustments that
462 reconciled the simulations with the experiments.

463 One challenge in developing models for bidirectional transport is how to incorporate the heterogeneous
464 motility observed for isolated DDB complexes (19,30,33). We tackled this issue by testing the effect of
465 DDB state switching in our simulations. In single-molecule TIRF experiments, Feng et al. quantified DDB
466 motility and found that DDB spends roughly two-thirds of the time in a processive minus-end directed
467 state, one third of the time in a stuck state, and a small fraction of time in a diffusive state (27). Including
468 this switching behavior in the simulation decreased the fraction of minus-end velocity events, but had a
469 weak effect on the population of fast plus-end velocity events. We conclude from this result that the large
470 experimental velocity peak centered around zero is likely not due to DDB residing predominantly in a stuck
471 state.

472 We found that incorporating a load-independent DDB detachment rate (an ideal bond) effectively
473 diminished the fast plus-end velocities seen in the simulations, better matching the experimental data.
474 This result can be understood simply as DDB remaining bound to the microtubule against the pulling forces
475 of kinesin, thus preventing durations in which DDB is detached and kinesin is moving at its unloaded speed.
476 This ideal bond is supported by experiments with activator-free dynein and with isolated vesicles, which
477 found evidence that dynein has catch-bond behavior under some conditions (slower detachment rate
478 with increasing load) (22,50). We note that a DDB optical trapping study by Elshenawy et al. did not find
479 evidence for catch-bond behavior of DDB (26). However, it remains a possibility that vertical forces
480 inherent to the single-bead optical trapping assay may contribute to detachment, as has been shown for
481 Kin-1 (23,26,57,60). Thus, our simulations put forth the testable hypothesis that when pulling exclusively
482 against hindering loads oriented parallel to the microtubule, DDB detachment is independent of load.

483 We found that incorporating a fast Kin-1 reattachment rate diminished the fast minus-end velocities in
484 the simulations, better matching the experimental data. This result can be understood simply as kinesin
485 reattaching rapidly following any detachment and thus minimizing the time that DDB moves at its
486 unloaded velocity. Our basic model used a $k_{reattach}$ value of 5 s^{-1}, which was initially determined in a study
487 that measured motor-driven deformations of giant unilamellar vesicles (46) and was later supported by
488 experiments that used DNA to connect two kinesins (44). Furthermore, this value has been employed in
489 a number of modeling studies (21). However, recent optical tweezer experiments found that against
490 hindering loads Kin-1 can slip backward in multiple 8 nm intervals and rapidly reengage with the
491 microtubule at rates consistent with our 50 s^{-1} reattachment rate (43,56,57). These experiments suggest
492 that against a hindering load parallel to the microtubule, Kin-1 enters a weak-binding state in which it slips
493 backward, and then rapidly reestablishes a strong-binding state. We also note that the reattachment rate
494 predicted from the bimolecular on-rate in solution and the effective tubulin concentration when two
495 motors are connected through a DNA linker is 125 s^{-1} (44). Thus, our simulations put forth the testable
496 hypothesis that when pulling against hindering loads oriented parallel to the microtubule, the Kin-1
497 reattachment rate is 50 s^{-1} or faster. A possible mechanism to explain this phenomenon is that if a kinesin
498 slips or detaches against a load oriented parallel to the microtubule, the motor is presented with multiple
499 sites of reattachment as it slides backward. Further, it is possible that if the motor reattaches against a
500 hindering load, the force enhances the rate of ADP release, which maximizes the probability that the
501 motor enters a strongly-bound state and restarts its walking cycle.

502 The second adjustment to the model that diminished the fast minus-end velocities was to increase the
503 stiffness of the linkage connecting the two motors. When model and experiments are compared by
504 analyzing instantaneous velocities, a 'recoil' effect becomes apparent following detachment of one of the
505 motors (usually kinesin in our simulations). For instance, using a 0.1 pN/nm stiffness of each motor, the
506 recoil of the cargo from a 5 pN force is 5 pN ÷ 0.1 pN/nm = 50 nm. Analyzed over a 100 ms instantaneous
507 velocity window, this displacement gives an apparent minus-end velocity of 500 nm/s. These fast minus-
508 end (or plus-end) instantaneous velocities were not seen in the experimental data that also used a 100
509 ms instantaneous velocity window (Fig. 2C). We found that increasing the motor stiffness to 0.2 pN/nm
510 eliminated the fast minus-end velocities in the simulations. Thus, the simulations provide a lower limit for
511 the motor stiffness and make the testable prediction that if a more compliant DNA linkage were used to
512 connect the motors, the instantaneous velocity distribution would reveal apparent fast velocities due to
513 large displacement recoil events.

514 Despite reconciling the simulations with the lack of fast plus- and minus-end velocities seen in the
515 experimental data, we still observed a small plus-end shift in the location of the simulated main velocity
516 peak relative to the experiments (Fig. 6B). Perhaps unsurprisingly, the position of this central velocity peak
517 was most influenced by the relative stall forces of DDB and Kin-1, highlighting that the antagonistic motors
518 rapidly establish a "draw" where each is pulling at near its maximum force. Reducing the Kin-1 stall force
519 from 8 pN to 6 pN shifted the peak towards zero, and reducing it further to 4 pN to match the 3.8 pN DDB
520 stall force shifted the simulated peak to nearly match the experiments (Fig. 5A). A large body of
521 experiments support a Kin-1 stall force in the range of 6 pN (22,38,51-55). However, another alternative
522 is the the DDB stall force is larger than 3.8 pN in this geometry. The DDB stall force was taken from a study
523 using single-bead tweezer geometry, and it is possible that in the geometry of these DDB-kinesin pairs
524 where forces are oriented solely parallel to the microtubule, the DDB stall forces are closer to the ~6 pN
525 of Kin-1. In principle, this hypothesis could be tested using a three-bead assay that minimizes vertical
526 forces inherent in the single-bead assay (57).

527 Despite the large body of single-molecule data describing their motor properties, it remains challenging
528 to predict the bidirectional dynamics that will result from antagonistic kinesin and dynein motor pairs. In
529 the present work, we find that using experimental data to constrain model simulations generates
530 mechanistic insights into how kinesin and DDB operate in antagonistic pairs. Our simulations support a
531 model in which: 1) in the range of forces generated by Kin-1, DDB detachment is independent of load; 2)
532 Kin-1 reattaches to the microtubule at 50 s^{-1} in the geometry of these motor pairs; and 3) when modeled

533 as linear springs, motor stiffness is at least 0.2 pN/nm. These model-generated hypotheses generate
534 testable predictions for future single-molecule experiments. Furthermore, by identifying motor
535 parameters that are the strongest determinants of bidirectional transport, this work provides a
536 framework to interpret how diverse kinesins, different activating dynein adapters, and motor-cargo
537 stiffness will affect the resulting bidirectional transport of intracellular cargo.

538

Author Contributions

T-C.M. and W.O.H. designed research, T-C.M. performed all simulations and carried out analysis, Q.F. and A.M.G. carried out experiments and carried out experimental data analysis. T-C.M., W.O.H. and A.M.G. wrote the manuscript, and all authors edited the manuscript.

Declaration of Interests

The authors declare no competing interests.

Acknowledgements

The authors thank George Ohashi and John Fricks who helped formulate a previous iteration of the current model, as well as members of the Hancock lab who provided helpful input. This work was supported by NIH grants R01GM076476 and R35GM139568 to W.O.H., and F32GM137487 to A.M.G.

References:

1. Encalada, S. E., L. Szpankowski, C. H. Xia, and L. S. B. Goldstein. 2011. Stable Kinesin and Dynein Assemblies Drive the Axonal Transport of Mammalian Prion Protein Vesicles. *Cell*. 144(4):551-565, doi: 10.1016/j.cell.2011.01.021.
2. Leidel, C., R. A. Longoria, F. M. Gutierrez, and G. T. Shubeita. 2012. Measuring Molecular Motor Forces In Vivo: Implications for Tug-of-War Models of Bidirectional Transport. *Biophysical Journal*. 103(3):492-500, doi: 10.1016/j.bpj.2012.06.038.
3. . !!! INVALID CITATION !!! (19-22).
4. Holzbaur, E. L., and Y. E. Goldman. 2010. Coordination of molecular motors: from in vitro assays to intracellular dynamics. *Current Opinion in Cell Biology*. 22(1):4-13, doi: 10.1016/j.ceb.2009.12.014.
5. Encalada, S. E., and L. S. B. Goldstein. 2014. Biophysical Challenges to Axonal Transport: Motor-Cargo Deficiencies and Neurodegeneration. *Annual Review of Biophysics*. 43(1):141-169, doi: 10.1146/annurev-biophys-051013-022746.
6. Hancock, W. O. 2014. Bidirectional cargo transport: moving beyond tug of war. *Nature Reviews Molecular Cell Biology*. 15(9):615-628, doi: 10.1038/nrm3853.
7. Goldstein, L. S. B. 2001. Kinesin molecular motors: Transport pathways, receptors, and human disease. *J Gen Physiol*. 118(1):4a-4a.
8. Eschbach, J., and L. Dupuis. 2011. Cytoplasmic dynein in neurodegeneration. *Pharmacol Therapeut*. 130(3):348-363, doi: 10.1016/j.pharmthera.2011.03.004.
9. Cai, D. W., K. J. Verhey, and E. Meyhofer. 2007. Tracking single kinesin molecules in the cytoplasm of mammalian cells. *Biophysical Journal*. 92(12):4137-4144, doi: 10.1529/biophysj.106.100206.
10. Courty, S., C. Luccardini, Y. Bellaiche, G. Cappello, and M. Dahan. 2006. Tracking individual kinesin motors in living cells using single quantum-dot imaging. *Nano Lett*. 6(7):1491-1495, doi: 10.1021/nl060921t.
11. Fridman, V., A. Gerson-Gurwitz, O. Shapira, N. Movshovich, S. Lakamper, C. F. Schmidt, and L. Gheber. 2013. Kinesin-5 Kip1 is a bi-directional motor that stabilizes microtubules and tracks their plus-ends in vivo. *Journal of Cell Science*. 126(18):4147-4159, doi: 10.1242/jcs.125153.
12. Gross, S. P., M. A. Welte, S. M. Block, and E. F. Wieschaus. 2000. Dynein-mediated cargo transport in vivo: A switch controls travel distance. *J Cell Biol*. 148(5):945-955, doi: 10.1083/jcb.148.5.945.
13. Ma, S., and R. L. Chisholm. 2002. Cytoplasmic dynein-associated structures move bidirectionally in vivo. *Journal of Cell Science*. 115(7):1453-1460.
14. Reck-Peterson, S. L., A. Yildiz, A. P. Carter, A. Gennerich, N. Zhang, and R. D. Vale. 2006. Single-Molecule Analysis of Dynein Processivity and Stepping Behavior. *Cell*. 126(2):335-348, doi: 10.1016/j.cell.2006.05.046.
15. Schnitzer, M. J., K. Visscher, and S. M. Block. 2000. Force production by single kinesin motors. *Nature Cell Biology*. 2(10):718-723, doi: 10.1038/35036345.
16. Visscher, K., M. J. Schnitzer, and S. M. Block. 1999. Single kinesin molecules studied with a molecular force clamp. *Nature*. 400(6740):184-189, doi: 10.1038/22146.
17. Dallon, J. C., C. Leduc, S. Etienne-Manneville, and S. Portet. 2019. Stochastic modeling reveals how motor protein and filament properties affect intermediate filament transport. *Journal of Theoretical Biology*. 464:132-148, doi: 10.1016/j.jtbi.2018.12.022.
18. Altaner, B., A. Wachtel, and J. Vollmer. 2015. Fluctuating currents in stochastic thermodynamics. II. Energy conversion and nonequilibrium response in kinesin models. *Phys Rev E*. 92(4), doi: 10.1103/PhysRevE.92.042133.

19. Puri, P., N. Gupta, S. Chandel, S. Naskar, A. Nair, A. Chaudhuri, M. K. Mitra, and S. Muhuri. 2019. Dynein catch bond as a mediator of codependent bidirectional cellular transport. *Physical Review Research*. 1(2), doi: 10.1103/physrevresearch.1.023019.
20. Ohashi, K. G., L. Han, B. Mentley, J. Wang, J. Fricks, and W. O. Hancock. 2019. Load-dependent detachment kinetics plays a key role in bidirectional cargo transport by kinesin and dynein. *Traffic*. 20(4):284-294, doi: 10.1111/tra.12639.
21. Muller, M. J. I., S. Klumpp, and R. Lipowsky. 2008. Tug-of-war as a cooperative mechanism for bidirectional cargo transport by molecular motors. *P Natl Acad Sci USA*. 105(12):4609-4614, doi: 10.1073/pnas.0706825105.
22. Kunwar, A., S. K. Tripathy, J. Xu, M. K. Mattson, P. Anand, R. Sigua, M. Vershinin, R. J. McKenney, C. C. Yu, A. Mogilner, and S. P. Gross. 2011. Mechanical stochastic tug-of-war models cannot explain bidirectional lipid-droplet transport. *P Natl Acad Sci USA*. 108(47):18960-18965, doi: 10.1073/pnas.1107841108.
23. Howard, J., and W. O. Hancock. 2020. Three Beads Are Better Than One. *Biophysical Journal*. 118(1):1-3, doi: 10.1016/j.bpj.2019.12.001.
24. Pyrpassopoulos, S., H. Shuman, and E. M. Ostap. 2020. Modulation of Kinesin's Load-Bearing Capacity by Force Geometry and the Microtubule Track. *Biophysical Journal*. 118(1):243-253, doi: 10.1016/j.bpj.2019.10.045.
25. Belyy, V., M. A. Schlager, H. Foster, A. E. Reimer, A. P. Carter, and A. Yildiz. 2016. The mammalian dynein–dynactin complex is a strong opponent to kinesin in a tug-of-war competition. *Nature Cell Biology*. 18(9):1018-1024, doi: 10.1038/ncb3393.
26. Elshenawy, M. M., J. T. Canty, L. Oster, L. S. Ferro, Z. Zhou, S. C. Blanchard, and A. Yildiz. 2019. Cargo adaptors regulate stepping and force generation of mammalian dynein–dynactin. *Nature Chemical Biology*. 15(11):1093-1101, doi: 10.1038/s41589-019-0352-0.
27. Feng, Q., A. M. Gicking, and W. O. Hancock. 2020. Dynactin p150 promotes processive motility of DDB complexes by minimizing diffusional behavior of dynein. *Molecular Biology of the Cell*. 31(8):782-792, doi: 10.1091/mbc.e19-09-0495.
28. Gutierrez, P. A., B. E. Ackermann, M. Vershinin, and R. J. McKenney. 2017. Differential effects of the dynein-regulatory factor Lissencephaly-1 on processive dynein-dynactin motility. *Journal of Biological Chemistry*. 292(29):12245-12255, doi: 10.1074/jbc.m117.790048.
29. King, S. J., and T. A. Schroer. 2000. Dynactin increases the processivity of the cytoplasmic dynein motor. *Nature Cell Biology*. 2(1):20-24, doi: 10.1038/71338.
30. McKenney, R. J., W. Huynh, M. E. Tanenbaum, G. Bhabha, and R. D. Vale. 2014. Activation of cytoplasmic dynein motility by dynactin-cargo adapter complexes. *Science*. 345(6194):337-341, doi: 10.1126/science.1254198.
31. Ross, J. L., K. Wallace, H. Shuman, Y. E. Goldman, and E. L. F. Holzbaur. 2006. Processive bidirectional motion of dynein-dynactin complexes in vitro. *Nature Cell Biology*. 8(6):562-570, doi: 10.1038/ncb1421.
32. Sanghavi, P., P. Kumar, A. Roy, M. S. Madhusudhan, and R. Mallik. 2021. On and off controls within dynein-dynactin on native cargoes. *P Natl Acad Sci USA*. 118(23), doi: 10.1073/pnas.2103383118.
33. Schlager, M. A., H. T. Hoang, L. Urnavicius, S. L. Bullock, and A. P. Carter. 2014. In vitro reconstitution of a highly processive recombinant human dynein complex. *The EMBO Journal*. 33(17):1855-1868, doi: 10.15252/embj.201488792.
34. Gillespie, D. T. 1977. Exact Stochastic Simulation of Coupled Chemical-Reactions. *J Phys Chem-Us*. 81(25):2340-2361, doi: 10.1021/j100540a008.

35. Coppin, C. M., D. W. Pierce, L. Hsu, and R. D. Vale. 1997. The load dependence of kinesin's mechanical cycle. *Proceedings of the National Academy of Sciences*. 94(16):8539-8544, doi: 10.1073/pnas.94.16.8539.
36. Bruno, L., M. Salierno, D. E. Wetzler, M. A. Despósito, and V. Levi. 2011. Mechanical Properties of Organelles Driven by Microtubule-Dependent Molecular Motors in Living Cells. *PLoS ONE*. 6(4):e18332, doi: 10.1371/journal.pone.0018332.
37. Oiwa, K., and H. Sakakibara. 2005. Recent progress in dynein structure and mechanism. *Curr Opin Cell Biol*. 17(1):98-103, doi: 10.1016/j.ceb.2004.12.006.
38. Andreasson, J. O. L., S. Shastry, W. O. Hancock, and S. M. Block. 2015. The Mechanochemical Cycle of Mammalian Kinesin-2 KIF3A/B under Load. *Current Biology*. 25(9):1166-1175, doi: 10.1016/j.cub.2015.03.013.
39. Andreasson, J. O., B. Milic, G.-Y. Chen, N. R. Guydosh, W. O. Hancock, and S. M. Block. 2015. Examining kinesin processivity within a general gating framework. *eLife*. 4, doi: 10.7554/elife.07403.
40. Bell, G. I. 1980. Theoretical-Models for the Specific Adhesion of Cells to Cells or to Surfaces. *Adv Appl Probab*. 12(3):566-567, doi: 10.1017/S0001867800035254.
41. Bell, G. I. 1978. Models for the specific adhesion of cells to cells. *Science*. 200(4342):618-627, doi: 10.1126/science.347575.
42. Arpag, G., S. Shastry, W. O. Hancock, and E. Tuzel. 2014. Transport by populations of fast and slow kinesins uncovers novel family-dependent motor characteristics important for in vivo function. *Biophys J*. 107(8):1896-1904, doi: 10.1016/j.bpj.2014.09.009.
43. Toleikis, A., N. J. Carter, and R. A. Cross. 2020. Backstepping Mechanism of Kinesin-1. *Biophysical Journal*. 119(10):1984-1994, doi: 10.1016/j.bpj.2020.09.034.
44. Feng, Q., K. J. Mickolajczyk, G. Y. Chen, and W. O. Hancock. 2018. Motor Reattachment Kinetics Play a Dominant Role in Multimotor-Driven Cargo Transport. *Biophys J*. 114(2):400-409, doi: 10.1016/j.bpj.2017.11.016.
45. Beeg, J., S. Klumpp, R. Dimova, R. S. Gracia, E. Unger, and R. Lipowsky. 2008. Transport of beads by several kinesin motors. *Biophysical Journal*. 94(2):532-541, doi: 10.1529/biophysj.106.097881.
46. Leduc, C., O. Campas, K. B. Zeldovich, A. Roux, P. Jolimaitre, L. Bourel-Bonnet, B. Goud, J. F. Joanny, P. Bassereau, and J. Prost. 2004. Cooperative extraction of membrane nanotubes by molecular motors. *P Natl Acad Sci USA*. 101(49):17096-17101, doi: 10.1073/pnas.0406598101.
47. Johnson, C. M. F. J. D. B., Anthony; Jung, P 2020. Dynamic catch-bonding generates the large stall forces of cytoplasmic dynein. *Physical Biology*. 17, doi: 10.1088/1478-3975/ab907.
48. Nair, A., S. Chandel, M. K. Mitra, S. Muhuri, and A. Chaudhuri. 2016. Effect of catch bonding on transport of cellular cargo by dynein motors. *Phys Rev E*. 94(3), doi: 10.1103/PhysRevE.94.032403.
49. Thomas, W. E., V. Vogel, and E. Sokurenko. 2008. Biophysics of catch bonds. *Annual Review of Biophysics*. 37:399-416, doi: 10.1146/annurev.biophys.37.032807.125804.
50. Rai, A. K., A. Rai, A. J. Ramaiya, R. Jha, and R. Mallik. 2013. Molecular Adaptations Allow Dynein to Generate Large Collective Forces inside Cells. *Cell*. 152(1-2):172-182, doi: 10.1016/j.cell.2012.11.044.
51. Svoboda, K., and S. M. Block. 1994. Force and Velocity Measured for Single Kinesin Molecules. *Cell*. 77(5):773-784, doi: 10.1016/0092-8674(94)90060-4.
52. Kawaguchi, K., and S. Ishiwata. 2000. Temperature dependence of force, velocity, and processivity of single kinesin molecules. *Biochem Bioph Res Co*. 272(3):895-899, doi: 10.1006/bbrc.2000.2856.

53. Gittes, F., E. Meyhofer, S. Baek, and J. Howard. 1996. Directional loading of the kinesin motor molecule as it buckles a microtubule. *Biophysical Journal*. 70(1):418-429, doi: 10.1016/S0006-3495(96)79585-1.
54. Hunt, A. J., F. Gittes, and J. Howard. 1994. The Force Exerted by a Single Kinesin Molecule against a Viscous Load. *Biophysical Journal*. 67(2):766-781, doi: 10.1016/S0006-3495(94)80537-5.
55. Budaitis, B. G., S. Jariwala, L. Rao, Y. Yue, D. Sept, K. J. Verhey, and A. Gennerich. 2021. Pathogenic mutations in the kinesin-3 motor KIF1A diminish force generation and movement through allosteric mechanisms. *J Cell Biol*. 220(4), doi: 10.1083/jcb.202004227.
56. Sudhakar, S., M. K. Abdosamadi, T. J. Jachowski, M. Bugiel, A. Jannasch, and E. Schaffer. 2021. Germanium nanospheres for ultraresolution picotensiometry of kinesin motors. *Science*. 371(6530):692-+, doi: 10.1126/science.abd9944.
57. Pyrpassopoulos, S., A. M. Gicking, T. M. Zaniewski, W. O. Hancock, and E. M. Ostap (2022). KIF1A is kinetically tuned to be a super-engaging motor under hindering loads. Cold Spring Harbor Laboratory.
58. Derr, N. D., B. S. Goodman, R. Jungmann, A. E. Leschziner, W. M. Shih, and S. L. Reck-Peterson. 2012. Tug-of-War in Motor Protein Ensembles Revealed with a Programmable DNA Origami Scaffold. *Science*. 338(6107):662-665, doi: 10.1126/science.1226734.
59. Monzon, G. A., L. Scharrel, A. Dsouza, V. Henrichs, L. Santen, and S. Diez. 2020. Stable tug-of-war between kinesin-1 and cytoplasmic dynein upon different ATP and roadblock concentrations. *Journal of Cell Science*. 133(22):jcs249938, doi: 10.1242/jcs.249938.
60. Khataee, H., and J. Howard. 2019. Force Generated by Two Kinesin Motors Depends on the Load Direction and Intermolecular Coupling. *Phys Rev Lett*. 122(18), doi: 10.1103/PhysRevLett.122.188101.

Supplementary:

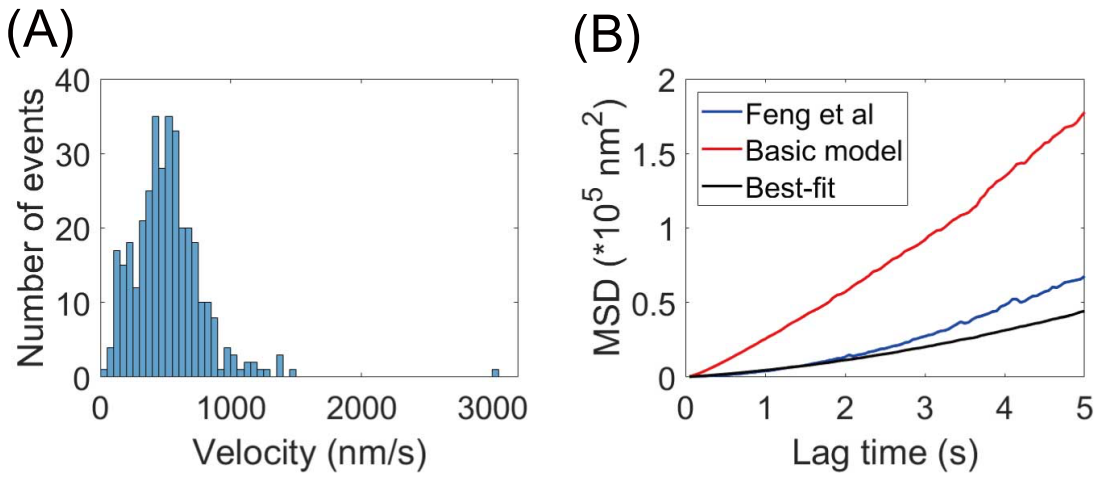

Figure S1. (A) Distribution of trace velocities of kinesin-1 alone in dynein motility buffer, which is used in Kin-DDB experiments (27). (Dynein motility buffer consists of 30 mM Hepes, 50 mM potassium acetate, 2 mM magnesium acetate, 1 mM EGTA and 10% glycerol, supplemented with 2 mg/ml casein, 20 mM glucose, 37 mM BME, glucose oxidase, catalase, 10 mM Taxol, and 2 mM ATP. Mean velocity is 515 nm/s, which was used for the unloaded kinesin-1 velocity in the simulations. (B) The mean squared displacement (MSD) curve of experimental data in Feng et al. (blue) (27), basic model (red), and best-fit model (black). In MSD analysis, the curves were fit with the equation: $MSD = V^2t^2 + 2Dt$, where V is velocity, D is the apparent diffusion coefficient, and t is lag time. Fit results are $V = 49\,nm/s, D = 996\,nm^2/s$ in experimental data, $V = 49\,nm/s, D = 11{,}800\,nm^2/s$ in basic model, and $V = 32\,nm/s, D = 1812\,nm^2/s$ in best-fit model.

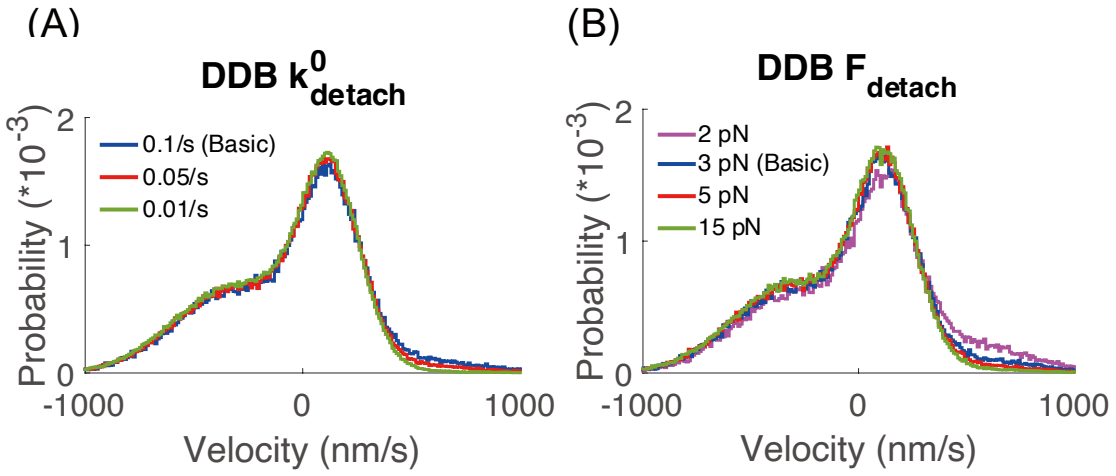

Figure S2. Effect of changing DDB detachment parameters on the instantaneous velocity distribution. (A) Effect of decreasing the unloaded DDB detachment rate was to weakly diminish the plus-end velocity peak. (B) Effect of increasing the DDB detachment force parameter was to moderately diminish the minus-end velocity peak, but was significant when increasing from 2 pN to 3 pN.

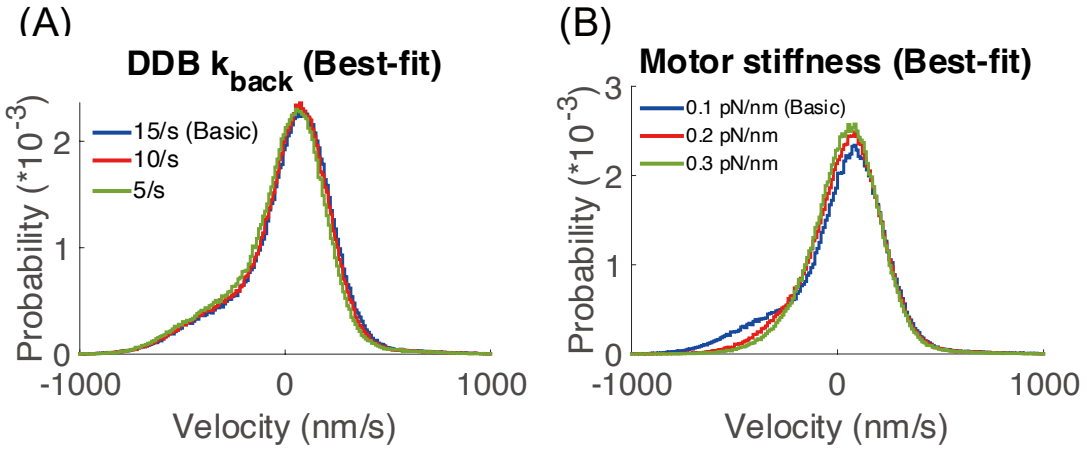

Figure S3. Instantaneous velocity distributions following implementation of ideal-bond for DDB, increasing the kinesin-1 reattachment rate to 50 s^{-1}, and reducing the kinesin-1 stall force to 6 pN. (A) Effect of altering the DDB backstepping rate, k_{back}, lightly shifted the mode peak toward zero. (B) Effect of increasing the motor stiffness was to reduce the minus-end velocity peak.

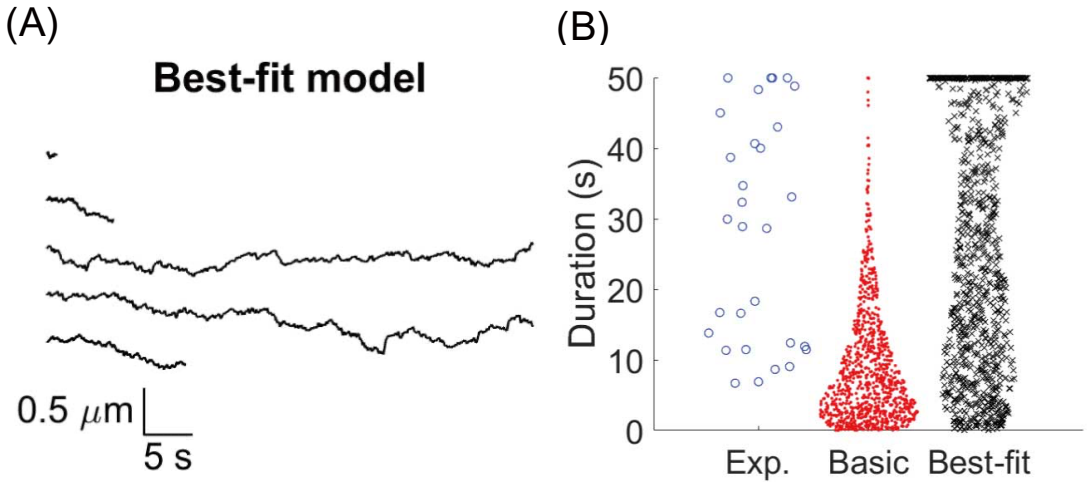

Figure S4. (A) Example traces of 50-second simulations of the best-fit model. (B) Distribution of run durations from experimental data (blue), basic model (red) and best-fit model (black). The best-fit model had longer run durations that more closely matched the experimental data.

745